Optical Engineering

OpticalEngineering.SPIEDigitalLibrary.org

Modulated dark-field phasing detection for automatic optical inspection

Heejoo Choi
John Mineo Kam
Joel David Berkson
Logan Rodriguez Graves
Dae Wook Kim

SPIE.

Heejoo Choi, John Mineo Kam, Joel David Berkson, Logan Rodriguez Graves, Dae Wook Kim, "Modulated dark-field phasing detection for automatic optical inspection," *Opt. Eng.* **58**(9), 092603 (2019), doi: 10.1117/1.OE.58.9.092603.

Modulated dark-field phasing detection for automatic optical inspection

Heejoo Choi,[a] John Mineo Kam,[a] Joel David Berkson,[a] Logan Rodriguez Graves,[a] and Dae Wook Kim[a,b,*]
[a]University of Arizona, James C. Wyant College of Optical Sciences, Tucson, Arizona, United States
[b]University of Arizona, Department of Astronomy and Steward Observatory, Tucson, Arizona, United States

Abstract. Dark-field illumination is a simple yet elegant imaging technique that can be used to detect the presence of particles on a specular surface. However, the sensitivity of dark-field illumination to initial conditions affects its repeatability. This is problematic in cases where automation is desired. We present an improvement to the current method of using a modulation field that relies on phase calculations rather than intensity. As a result, we obtain a computational method that is insensitive to noise and provides clearly defined particle information, allowing a global threshold to be set for autonomous measurement purposes. After introducing the theory behind our method, we present experimental results for various scenarios and compare them to those obtained using the dark-field approach. © *2019 Society of Photo-Optical Instrumentation Engineers (SPIE)* [DOI: 10.1117/1.OE.58.9.092603]

Keywords: automatic optical inspection; particle detection; dark field; phase measurement.

Paper 190052SS received Jan. 13, 2019; accepted for publication Mar. 4, 2019; published online Mar. 26, 2019.

1 Introduction

Fabrication of semiconductors and display panels is a cutting-edge and competitive industry in which products must be manufactured reliably, with minimal defects, and in high volumes to maximize profit margins. Manufacturers implement automatic optical inspection (AOI) processes[1–3] to interpret the results of continuous repetitive inspections with minimal human interaction. As this is an automated process, reliable thresholds must be set to distinguish bad products from good ones.

The difficulty in AOI lies in detecting small defects over a large area in a dynamic environment. This kind of scenario is often found in lithography processes applied to semiconductors or display panels, where the wire grid is incorrectly patterned on the wafer because of defects on the surface of the masks or substrates.[4,5] The substrates (wafers) are typically greater than 100 mm in diameter (sometimes reaching 1 to 2 m depending on the facility), yet particles on the order of microns can result in errors. Inspection using human knowledge might provide more trustworthy results but will require much longer inspection times. To meet the needs of industry, a robust AOI that produces reliable results and minimizes runtime is essential.

Dark-field illumination[6–10] is one of the simplest and most powerful solutions among current methods of detecting particles on substrates and masks. This method produces a high-contrast image in which objects of interest appear bright atop a dark background. The images are achieved by illuminating the specular surface at a grazing angle, with the detector placed almost normal to the surface of the unit under test (UUT). In this configuration, only light that has been scattered by particles or defects on or in the surface can reach the detector.[7,8] This method is often associated with the microscopy of biological samples, where the sample itself is sometimes transparent and the scattered light from the object produces a nice high-contrast image.[6,9,10]

In measurements where high repeatability and automation is needed, relying on the inherently noisy intensity is not ideal. The effectiveness of intensity data depends on the roughness and orientation of the particle scattering the light, as well as the signal-to-noise ratio (SNR). If the AOI threshold for judging particles is fixed, the results will vary from trial to trial because of changes in measurement conditions or even Gaussian noise in the sensor itself.

This paper describes a new method of inspection that instead relies on phase differences to detect small defects on a specular surface. In Sec. 2, we introduce the proposed modulated field (MF) method. Section 3 describes a case study of various initial phase differences, before Sec. 4 presents the result of an experimental comparison between the proposed method and the conventional dark-field approach. Finally, the conclusions to this study are summarized in Sec. 5.

2 Modulated Dark-Field Detection

2.1 *Modulated Dark-Field System Configuration*

Our method, known as MF illumination, uses a similar setup to that used in the dark-field case but considers the phase rather than the intensity to distinguish the target from the background. This is achieved through the addition of a second light source (LCD monitor) located almost normal to the surface that illuminates the entire surface, as shown in Fig. 1.

Each light source is driven to produce a time-varying sinusoid (brightness changes with time). The key lies in phase shifting the signals such that the grazing LED produces a signal that is out of phase with that produced by the monitor normal to the UUT's surface. After image processing, the pixel values correspond to the newly defined phase-index, in which the particles and background have different, specific values. This phase information provides stable

*Address all correspondence to Dae Wook Kim, E-mail: letter2dwk@hotmail.com

0091-3286/2019/$25.00 © 2019 SPIE

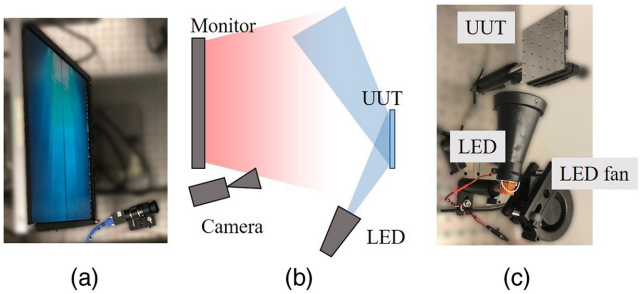

Fig. 1 (a) Camera and monitor. (b) UUT, LED, and LED fan for cooling. (c) Schematic diagram of experimental setup. All rays from the LED reflect off the specular surface of the UUT, except those scattered by defects on the surface. The rays from the monitor fill the surface of the UUT with uniform phase information, except in areas where defects occur.

results, even if the particle intensity values are low, as the calculated phases are the same for every particle [see Fig. 2(a)]. This allows for simple criteria to be used in determining a threshold that yields reliable and repeatable results without any human interaction. In addition, if there is an intensity-sensitive mark (e.g., mask pattern) on the UUT, this mark will show up in the intensity difference map but not in the phase map, as shown in Fig. 2(b).

2.2 *Detection Criteria Using Phase-Index Value*

When assigning different phases to the LED and the screen to achieve a phase contrast, our options are only limited by the precision of the brightness used to drive each element. However, as our goal is to obtain a high phase contrast between the background and particle, we opt to produce the largest possible phase difference.

When we take the image, some pixels may record the physical boundary of the particle. Thus, the issue of the fill factor must be considered. The particle (30 to 50 μm) could occupy several pixels on the sensor (4 to 10 pixels), and these pixels on the sensor will record blended information of the background and particles. A pixel might have a fully occupied signal from either light source, or contain some fraction of both. Such a blended case with mixed signals is simulated using

$$I_{\text{particle}}(x,y,n) = A_1(x,y)\sin\left(\frac{\pi n}{N} + \Phi_1\right), \tag{1}$$

$$I_{\text{background}}(x,y,n) = A_2(x,y)\sin\left(\frac{\pi n}{N} + \Phi_2\right), \tag{2}$$

$$\Phi_{\text{index}}(x,y) = a\tan Q\left[\frac{\sum_{n=1}^{N} I(x,y,n)\sin\left(\frac{2\pi n}{N}\right)}{\sum_{n=1}^{N} I(x,y,n)\cos\left(\frac{2\pi n}{N}\right)}\right], \tag{3}$$

where I_{particle} is the intensity from light scattered by a particle and $I_{\text{background}}$ is the intensity reflected by the specular back surface. A_1 and A_2 are the fill factors for each signal ($A_1 + A_2 = 1$), which take account of the case of a mixed signal (e.g., boundary of particle or particle smaller than the resolution of our camera). N is the total number of phase steps and n is the index of the step number (e.g., $n = 1-4$. Φ_1 and Φ_2 denote the initial phase of each source. We can insert any pair of Φ_1 and Φ_2 so that the resulting map has a high contrast. Note that the goal of this calculation and treatment is to obtain a high-contrast map in which particle information can be easily distinguished from nonparticle information. $I(= I_{\text{particle}} + I_{\text{background}})$ in Eq. (3) is the recorded value (mixed intensity) used to compute the ensemble phase-index Φ_{index}. The mixed intensity I is recorded for every single pixel (x, y) and all the data processing calculations are performed pixel by pixel.

The phase-index $\Phi_{\text{index}}(x,y)$ is calculated from the four-quadrant inverse tangent ($a\tan Q$) from Eq. (3) using the intensity variation during the phase stepping ($n = 1,2,3,\cdots,N$). It is important to use the four-quadrant inverse tangent, because this can distinguish the sign of the numerator and denominator in the parentheses in Eq. (3), resulting in a phase range of $[-\pi, \pi]$. The normal arctangent

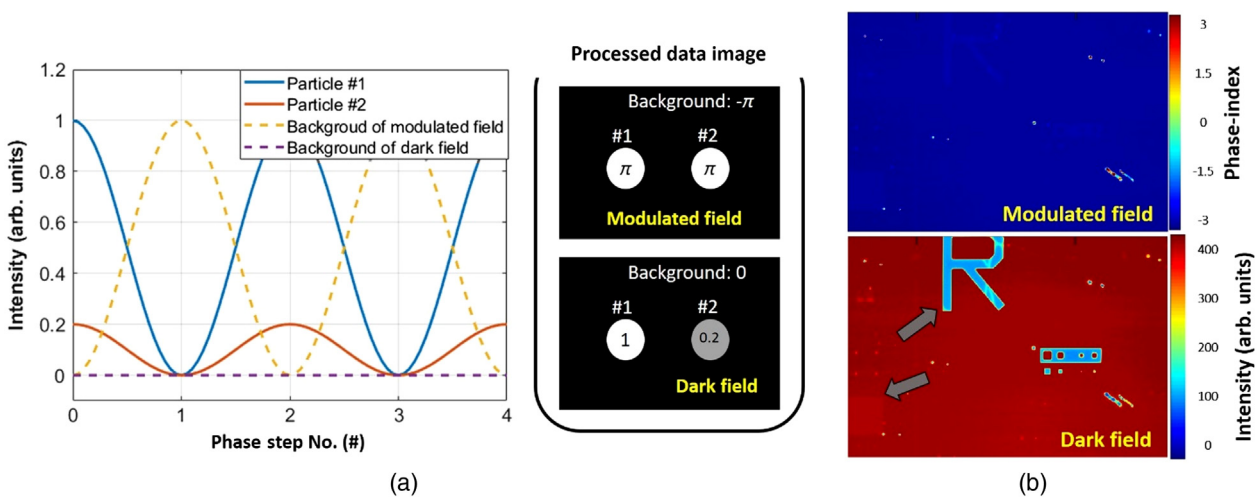

Fig. 2 The benefit of MF calculations. (a) Schematic diagram of the processed data image. MF method shows the same phase-index difference for different intensity variation cases (particles #1 and #2). (b) Measured data using MF (top) and dark-field (bottom) methods on a sample with mask patterns (gray arrows). MF method applies the same phase contrast to both background and mask patterns with the particle signals. The intensity-based dark-field measurement suffers from the reflectance given by the mask patterns.

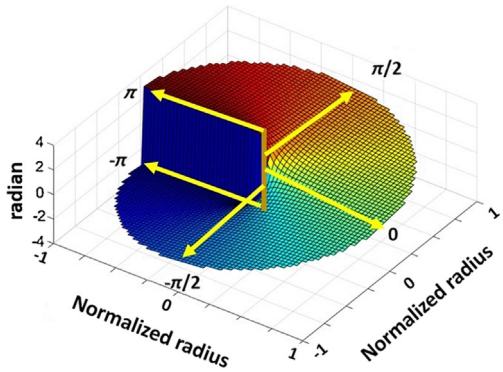

Fig. 3 Maximized angular range space of the phase-index using the four-quadrant inverse tangent. We can calculate the phase-index value based on the measured intensity variation at every single pixel during the phase-stepping process.

calculation does not account for the sign of the numerator and denominator, and so only produces values in the range $[-\pi/2, \pi/2]$. For instance, $a\tan(-1/4)$ and $a\tan(1/-4)$ give the same result. In contrast, using $a\tan Q$ enables us to calculate the phase-index over the maximum range of angle information, as shown in Fig. 3.

3 Case-Study Simulation for Different Initial Phase Comparison

The value given by Eq. (3) will be mapped to the angular phase space of Fig. 3 as a single phase-index angle. Because some pixels record the mixed intensity from the two light sources, the phase-index may have a middle value between the extreme cases (pure-particle and pure-background). To ensure the clear detection of particles, it is computationally preferable for the middle phase values to have a clear bimodal distribution, which directly depends on the two initial phase values Φ_1 and Φ_2 in Eqs. (1) and (2).

Table 1 Four exemplary Φ_1 and Φ_2 combinations.

	Case 1	Case 2	Case 3	Case 4
Φ_1	$-\pi/4$	0	0	$\pi/2$
Φ_2	$\pi/4$	$\pi/2$	π	$-\pi/2$
$\lvert\Phi_1 - \Phi_2\rvert$	$\pi/2$	$\pi/2$	π	π

Table 1 lists four exemplary Φ_1 and Φ_2 combinations that can be used to demonstrate the dependency. In Fig. 4, the variation of the final phase-index values is presented as a function of the contribution of the scattered particle intensity into a single pixel signal. In other words, 100% denotes the pure particle signal and 0% denotes the background signal only. Though all cases could be used for the phase-index calculation, to achieve a highly bimodal distribution with a clear distinction between the particle and the background cases, case 1 ($\Phi_1 = -\pi/4$ and $\Phi_2 = \pi/4$) is used to provide the performance evaluation results presented in the remainder of this paper.

If we examine the phase variation trend with respect to the fill factor, unlike the monotonically changing phase-index value for case 2, which has a continuous distribution, case 1 provides the highest contrast (i.e., discontinuity with 2π jump) at the mixed phase region around the 50% fill factor. This is even larger than the phase-index difference in the two extreme cases ($4\pi/3$ between the 0% and 100% fill factor case) in Fig. 4. This clear distinction between the particle-dominant and background-dominant cases offers a simple and robust threshold value for an AOI implementation.

Cases 3 and 4 are worth discussing, as they have only two step values (case 3: π and 0, case 4: $\pi/2$ and $-\pi/2$) rather than varying phase-index values as a function of the fill factor. Although this appears to offer a convenient contrast for an AOI application, it is easily affected by noise around the 50% fill factor. For instance, in case 3, two signals mixed in a single pixel are effectively $A_1 \sin(x) + A_2 \sin(x + \pi)$, and the similar A_1 and A_2 values from the 50% fill factor situation yield a sinusoidal signal with almost zero amplitude, which could induce a poor SNR. Thus, the final phase-index value is not robust and reliable as an AOI threshold.

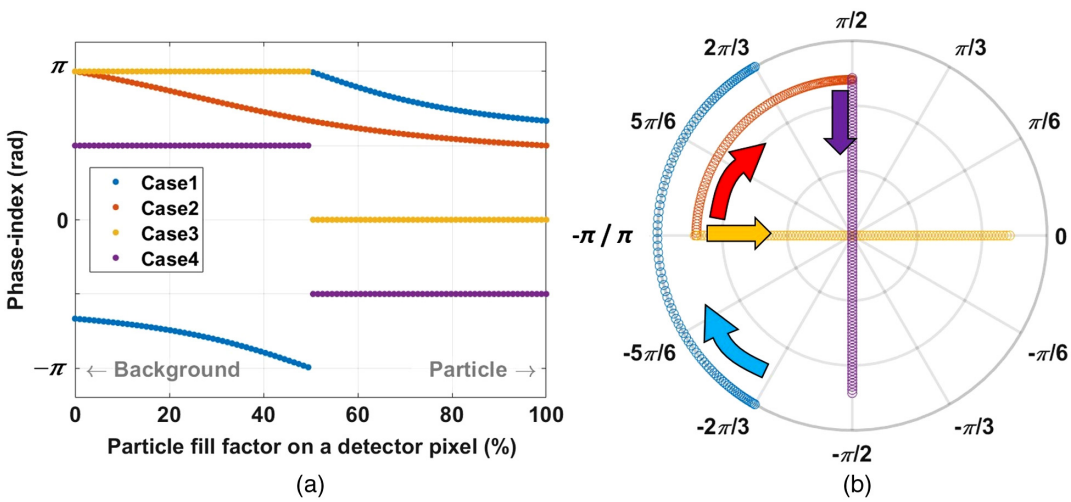

Fig. 4 (a) Phase-index calculation results as a function of the particle fill factor on a detector pixel signal. (b) Phase variation on a polar plot, showing the bimodal jump when the fill factor is exactly 50%. The arrow indicates the direction of the phase change as the contribution of the particle fill factor increases. The radial value (amplitude) of each sampling point is scaled arbitrarily to visualize the change in the calculated phase-index value.

Another interesting aspect is when we have two very small initial phase values with opposite signs, such as $\Phi_1 = -0.001\pi$ and $\Phi_2 = 0.001\pi$. While this works perfectly well in ideal simulation cases, in practical applications with noise in the raw data, the total signal across all the fill factor values is simply too small and well below the noise level. In this case, we are subject to similar limitations as the dark-field approach, where we are restricted by the overall SNR during the data processing stage.

4 Experimental Performance Demonstration

4.1 *Performance Comparison*

The four cases listed in Table 1 were experimentally tested and verified alongside the standard dark-field method using the setup shown in Fig. 1. We used an off-the-shelf monitor (Dell 1907FP) and camera (Pointgrey, FL3-U3-13Y3M-C), as well as a three-point emitting LED (Cree LEDs, XHP 35) driven by an Arduino controller to produce the required modulated signal. The camera was placed 55 cm from the sample UUT, which was the Al-coated mirror shown in Fig. 5. Under these conditions, a single detector pixel occupied an area of $\sim 80 \times 80$ μm on the sample. To create a constant reference sample, we sprayed a clean surface with particles of a known size. A polycrystalline particle spray (Struers, DP-Spray P 35 μm) was used to deposit equal-sized particles ($\sim$35 μm) on the surface of the Al-coated UUT.

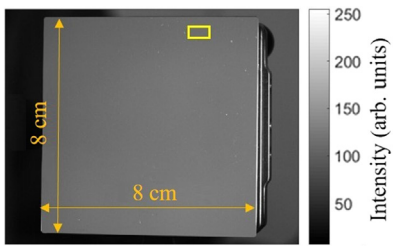

Fig. 5 Detector image of the Al-coated mirror surface of the UUT. This is one of the raw images from the eight phase shifts (i.e., $N = 8$). The yellow box indicates the region of the data comparisons in Figs. 6–8.

For the four MF cases, as predicted from the simulation study, case 1 produces the best contrast and clear particle boundaries in the calculated map. Case 2 fails to provide good-quality phase information because of the low contrast between the particle and background signals. In contrast, cases 3 and 4 give gradually changing phase-index values near the particle boundary, because the boundary is less clear (compared with the large 2π phase step in case 1) in the phase-index space (see Fig. 4) in the presence of actual measurement noise such as Gaussian white noise. In addition, these cases are similar to the dark-field result (bottom of Fig. 6), which suffers from a fuzzy intensity change near the particle boundary. This highlights the robustness of case 1 in the practical application of the MF approach. Therefore, the optimal initial phase values of the MF approach defined in Eq. (3) are $\Phi_1 = -\pi/4$ and $\Phi_2 = \pi/4$ (case 1), as they provide the sharpest AOI distinction criteria with a high-contrast particle map.

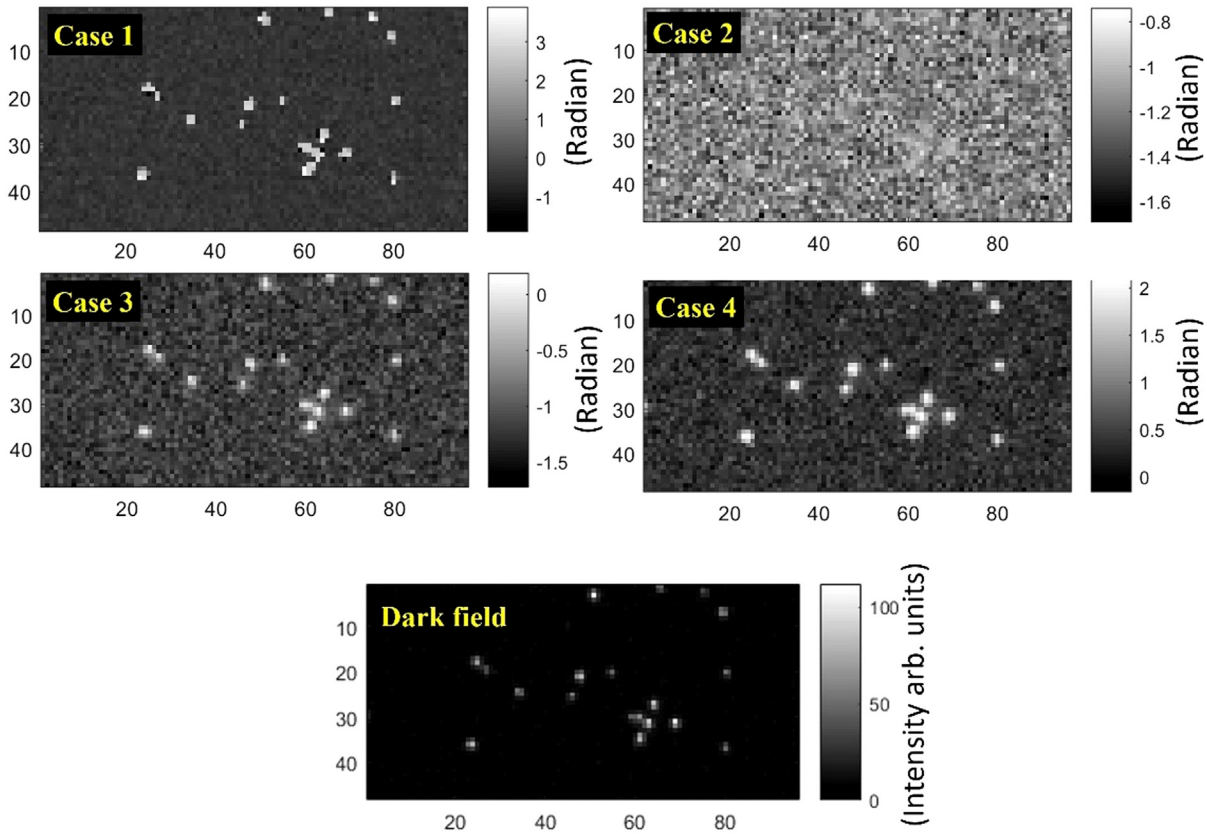

Fig. 6 Experimental results for cases 1–4 using the MF method and for the dark-field case. The x- and y-axes represent the pixel number (location) on the detector.

The sensitivity obtained from dark-field measurements can be improved by increasing the brightness of the LED, but this does not mean that a uniform signal will be received from all particles. The mask pattern, which has high reflectance, will also affect the results in this case. At the same time, increasing the signal from the particles always improves the signals received in the phase measurements. Hence, for a given hardware configuration, the MF approach yields more objective inspection results than the dark field in a realistic environment.

4.2 *Automatic Optical Inspection Performance*

Next, we adjusted the phase deviation and LED brightness to obtain the optimal results from the MF and dark-field methods, respectively, for a reliability test. A total of 10 trials were conducted to check the repeatability of the methods, with 10 snapshots taken in each trial for averaging purposes. To ensure a fair evaluation, the total number of snapshots for each case was fixed (for each trial, MF: 10 snaps ×8 modulations, dark field: 40 snaps ×2 for LED on and off).

The results from one of the trials are shown in Fig. 7(a) and the associated statistical distribution is shown in Fig. 7(b). To give a clear view of the particle, we used inverted images during the data processing step. There is a stark contrast between particle and background in the phase-index map, whereas the dark-field measurement produces an ambiguous particle boundary. For an AOI to determine the presence (and/or size) of a particle, it is critical to generate the normalized map using a certain threshold value, but this is often based on subjective human intuition. The MF method offers a much wider range of safe threshold values when creating an AOI than in the dark-field case. Any fluctuations in noise do not severely disturb the results in the MF. However, because of the fluctuating results in the dark field, human intervention will often be needed to set the threshold and verify the results.

The AOI algorithm categorizes a particle based on the threshold chosen from the histogram plot. When implementing the dark-field approach, even if a threshold value is carefully chosen for one trial, fluctuations between trials may change the intensity distribution. The green error bars in Fig. 7(b) show the fluctuations in the intensity distribution over the 10 trials. The top histogram in Fig. 7(b) clearly demonstrates the additional stability that the MF approach offers over the intensity-based dark-field results (bottom), indicating a high-fidelity method. In other words, the modulated

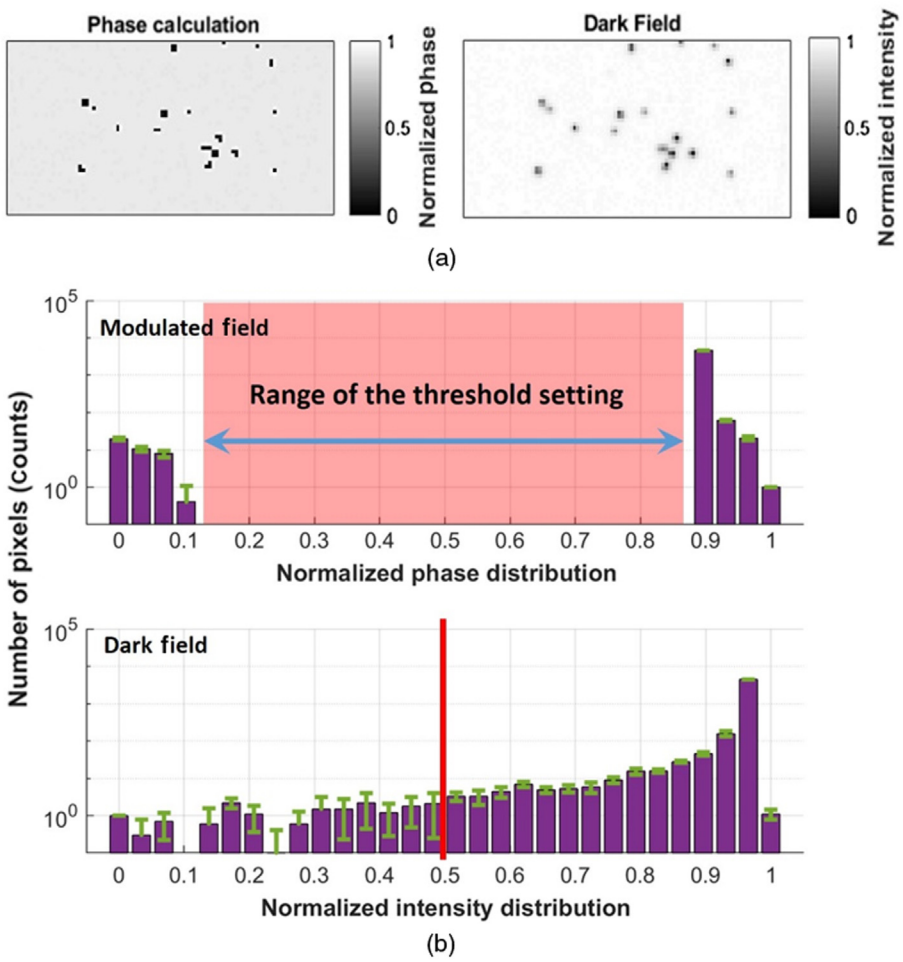

Fig. 7 Comparison of particle detection measurement results from the different methodologies. (a) Image from a single trial. The MF method (left) clearly produces distinguishable particle information, unlike the dark-field result (right), which gives an unclear boundary. (b) Histogram of the pixel value distribution, showing the phase-index (top) and intensity (bottom) from all pixels. The possible range of threshold settings is shown in the red zone.

Fig. 8 AOI defect detection percentage (%) results for (a) MF and (b) dark-field measurements. In the case of a fixed threshold value, the dark-field method failed to detect three particles, two completely (red arrow) and one 60% of the time (blue arrow), whereas the MF AOI was able to detect all one particle, which was still detected 90% of the time.

dark-field phasing detection enables an enhanced robustness of the AOI method against random noise in the actual measurement signal. However, we also acknowledge that this does not mean a 100% immunity to such noise. Just like other systems with uncertainties, there is still a chance, albeit small, for false-positives and missed particles depending on the actual magnitude of the noise and the intrinsic errors of the built system.

Figure 8 represents the results of a fixed (constant) threshold AOI over the 10 trials. While most particles were repeatedly detected in the MF method (one particle missed in one of the ten trials), the dark-field method failed to detect three particles (red and blue arrows) with high fidelity. A lower threshold value could have been set to allow the dark-field AOI to detect the missing particles, but this may result in false positives depending on the noise levels.

5 Conclusion

Using modulated phase information in addition to the previously established dark-field method, we have developed a reliable particle detection method called MF detection. Under noisy or dynamic testing environments (e.g., room light and reflectance of the substrate), a single parameter setting (e.g., brightness of light sources and threshold for judgment of particles) might not produce optimal or universal solutions. The MF approach provides more robust results than the dark-field approach at the expense of an additional LCD screen, as it does not require a tightly controlled testing environment or skilled human input.

Acknowledgments

This research was made possible in part by the II-VI Foundation Block-Gift Program and the Technology Research Initiative Fund Optics/Imaging Program. The authors wish to thank Spectral Optics for the use of their equipment.

References

1. H. Golnabi and A. Asadpour, "Design and application of industrial machine vision systems," *Rob. Comput. Integr. Manuf.* **23**, 630–637 (2007).
2. K. Harding, *Handbook of Optical Dimensional Metrology*, Chapter 2, CRC Press, Boca Raton, Florida (2013).
3. E. N. Malamas et al., "A survey on industrial vision systems, applications and tools," *Image Vision Comput.* **21**(2), 171–188 (2003).
4. H. Rau and C. H. Wu, "Automatic optical inspection for detecting defects on printed circuit board inner layers," *Int. J. Adv. Manuf. Technol.* **25**(9–10), 940–946 (2005).
5. D. M. Tsai and C. Y. Hung, "Automatic defect inspection of patterned thin film transistor-liquid crystal display (TFT-LCD) panels using one-dimensional Fourier reconstruction and wavelet decomposition," *Int. J. Prod. Res.* **43**(21), 4589–4607 (2005)
6. S. H. Gage, "Modern dark-field microscopy and the history of its development," *Trans. Am. Microsc. Soc.* **39**(2), 95–141 (1920).
7. M. Feldman and O. W. Lynn, "Inspection system utilizing dark-field illumination," U.S. Patent 4,595,289 (1986).
8. G. Addiego, "Automated specimen inspection system for and method of distinguishing features or anomalies under either bright field or dark field illumination," U.S. Patent 5917588A (1999).
9. K. Maslov, G. Stoica, and L. V. Wang, "In vivo dark-field reflection-mode photoacoustic microscopy," *Opt. Lett.* **30**(6), 625–627 (2005).
10. P. T. Goedhart et al., "Sidestream dark field (SDF) imaging: a novel stroboscopic LED ring-based imaging modality for clinical assessment of the microcirculation," *Opt. Express* **15**(23), 15101–15114 (2007).

Heejoo Choi is a postdoctoral researcher at James C. Wyant College of Optical Sciences at the University of Arizona. He has studied nonlinear optical harmonic generation and optical metrology. His current research mainly focuses on the development of optical metrology for science and industry.

John Mineo Kam is a master's student in the James C. Wyant College of Optical Sciences at the University of Arizona. He has a background in physics, building interferometry systems to test the alignment of surfaces. His work in optical metrology continues in the Large Optics Fabrication and Testing group, where he works on new deflectometry techniques to surpass traditional systems limited by the surface figure of the unit under test.

Joel David Berkson is a senior undergraduate student studying optical sciences and engineering at the University of Arizona. He is beginning his PhD in the fall of 2019. His main research interests include deflectometry, optical system design, and image science.

Logan Rodriguez Graves is a PhD candidate in the James C. Wyant College of Optical Sciences at the University of Arizona. His main research area covers precision optical metrology, focusing on deflectometry hardware and software development for improved freeform measurement capabilities. He also has a background in biomedical engineering, with research topics including early cancer detection utilizing autofluorescence and nonlinear rod–cone interactions at the retinal level.

Dae Wook Kim is an assistant professor of optical sciences and astronomy in the James C. Wyant College of Optical Sciences at the University of Arizona. His research area covers precision optical engineering including interferometry and deflectometry. He is the chair of the Optical Manufacturing and Testing (SPIE) and Optical Fabrication and Testing (OSA) conferences. He is a senior member of OSA and SPIE and has been serving as an associate editor for *Optics Express*.